

**NOTICE OF COPYRIGHT**

This manuscript has been authored by UT-Battelle, LLC under Contract No. DE-AC05-00OR22725 with the U.S. Department of Energy. The United States Government retains and the publisher, by accepting the article for publication, acknowledges that the United States Government retains a non-exclusive, paidup, irrevocable, world-wide license to publish or reproduce the published form of this manuscript, or allow others to do so, for United States Government purposes. The Department of Energy will provide public access to these results of federally sponsored research in accordance with the DOE Public Access Plan(<http://energy.gov/downloads/doepublicaccess-plan>).

# Destabilization of magnetic order in a dilute Kitaev spin liquid candidate

P. Lampen-Kelley,<sup>1,2</sup> A. Banerjee,<sup>3</sup> A.A. Aczel,<sup>3</sup> H.B. Cao,<sup>3</sup> J.-Q. Yan,<sup>2</sup> S.E. Nagler,<sup>3</sup> and D. Mandrus<sup>1,2</sup>

<sup>1</sup>*Department of Materials Science and Engineering,  
University of Tennessee, Knoxville, TN 37996, U.S.A.*

<sup>2</sup>*Materials Science and Technology Division, Oak Ridge National Laboratory, Oak Ridge, TN, 37831, U.S.A.*

<sup>3</sup>*Quantum Condensed Matter Division, Oak Ridge National Laboratory, Oak Ridge, TN 37831, U.S.A.*

(Dated: December 21, 2016)

Quantum fluctuations in a 2D honeycomb Kitaev model completely suppress long-range order to produce a quantum spin liquid (QSL) ground state. While  $\alpha$ - $\text{RuCl}_3$  is positioned on the verge of the Kitaev QSL phase, fragile long-range magnetic order arises from non-Kitaev terms in the Hamiltonian. In a study of  $\text{Ru}_{1-x}\text{Ir}_x\text{Cl}_3$  single crystals, we find that spin vacancies in the form of nonmagnetic  $\text{Ir}^{3+}$  successfully destabilize magnetic order in  $\alpha$ - $\text{RuCl}_3$ . Neutron diffraction and bulk characterization demonstrate a suppression of the primary zig-zag magnetic phase transition in  $\text{Ru}_{1-x}\text{Ir}_x\text{Cl}_3$  single crystals to below 2 K by  $x = 0.09$ , potentially paving the way towards the sought-after pure Kitaev limit. Stacking disordered regions exhibit less sensitivity to dilution, and sustain weak zig-zag correlations to larger  $x$ , near the percolation threshold for the honeycomb lattice. The phase diagram as a function of  $x$  and  $T$  is determined.

PACS numbers: 75.30.Kz, 75.10.Kt

The quantum spin liquid (QSL) holds particular fascination as a state of matter that exhibits strong quantum entanglement yet is devoid of long-range order [1, 2]. These exotic states can possess topologically protected fractionalized excitations, with possible implications for quantum information science [3, 4]. A prototypical example is the Kitaev model on a honeycomb lattice[5], which can be solved exactly and has a QSL ground state. An effective Hamiltonian with Kitaev terms consisting of bond-directional Ising couplings can arise in spin-orbit assisted Mott insulators with  $J_{eff} = 1/2$  moments in an edge-sharing octahedral environment [6]. A strong push for the experimental realization of quasi-2D honeycomb lattices showing Kitaev physics initially focused on iridate materials with chemical formula  $\text{A}_2\text{IrO}_3$  [7–10], and more recently there has been much interest in  $\alpha$ - $\text{RuCl}_3$ [11–14]. Each of these compounds orders magnetically at low temperatures in a zig-zag or incommensurate phase [15–21], and the effective low energy Hamiltonian is believed to be described by a generalized Heisenberg-Kitaev- $\Gamma$  model [22–33]. Despite the appearance of long-range order, broad scattering continua observed via inelastic neutron or Raman scattering in  $\alpha$ - $\text{RuCl}_3$  [13, 34–36] and the iridates [37] match the predicted signatures of itinerant Majorana fermions in pure Kitaev calculations [38–40], suggesting that Kitaev interactions play an important role in these materials and that they are proximate to the QSL state.

In this letter we report the evolution of the magnetic ground state in  $\alpha$ - $\text{RuCl}_3$  with magnetic  $\text{Ru}^{3+}$  substituted by nonmagnetic  $\text{Ir}^{3+}$ , and determine a complete phase diagram as a function of temperature and dilution. The motivation to understand the response of QSL-adjacent systems to perturbations is two-fold: first, to account for the role of unavoidable defects in real materials and secondly, to explore avenues towards suppression of long-range order and the realization of the pure QSL or other

exotic states. Numerous theoretical studies predict the emergence of novel superconductivity with hole doping in the strong Kitaev limit [41–48] while bond disorder [49], dislocations [50], magnetic impurities [51], and spin vacancies [52–57] have also received theoretical attention. Experimentally, substitution of both magnetic and non-magnetic cations for Ir rapidly led to spin glass freezing in  $\text{Na}_2\text{IrO}_3$  and  $\text{Li}_2\text{IrO}_3$  [58, 59]. Isoelectronic substitution within the solid solution  $(\text{Na,Li})_2\text{IrO}_3$  decreased the magnetic ordering temperature, although phase separation has hampered efforts to completely suppress long-range order [60–62].

With no intervening alkaline earth cation between layers, the chemically simpler binary compound  $\alpha$ - $\text{RuCl}_3$  provides an excellent framework to explore the effects of various perturbations on the relevant Kitaev physics. Low-spin  $5d^6$   $\text{Ir}^{3+}$  ( $S = 0$ ) represents a non-magnetic impurity in the  $J_{eff} = 1/2$   $\text{Ru}^{3+}$  magnetic sublattice while the identical ionic radii (0.68 Å) of  $\text{Ru}^{3+}$  and  $\text{Ir}^{3+}$  preserve a regular  $\text{MCl}_6$  environment.

The weakly van der Waals bonded honeycomb layers in  $\alpha$ - $\text{RuCl}_3$  are very susceptible to stacking faults, and these are known to affect the magnetic properties. Two zig-zag magnetic phases, distinguished by out-of-plane periodicity (ABC vs ABAB) and  $T_N$  (7 K vs 14 K) can be observed depending on growth conditions and sample history [13, 14, 20, 21]. Single crystals with pristine monoclinic stacking exhibit a single 7 K transition, while the appearance of a second transition at 14 K is associated with the presence of stacking faults [21]. In  $\text{Ru}_{1-x}\text{Ir}_x\text{Cl}_3$  we observe a rapid suppression of the 7 K (ABC-type) zig-zag antiferromagnetic transition of the clean  $\alpha$ - $\text{RuCl}_3$  system with increasing  $x$ , demonstrating that site dilution represents a viable approach to destabilizing long-range magnetic order.  $\text{Ru}_{1-x}\text{Ir}_x\text{Cl}_3$  also exhibits a secondary magnetic phase of ABAB type that is less sensitive to Ir content and completely suppressed

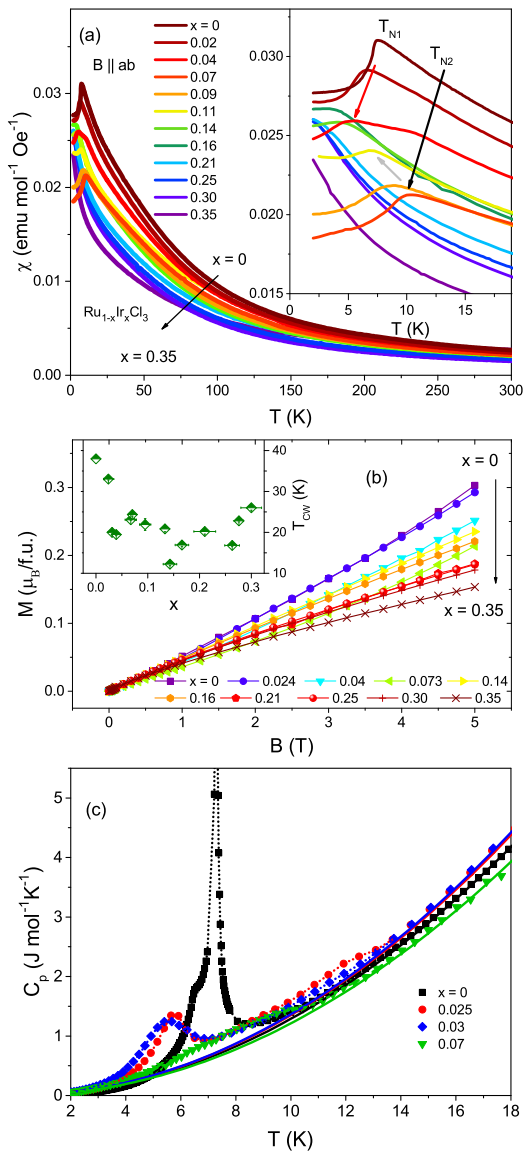


FIG. 1. (a) Magnetic susceptibility curves of  $\text{Ru}_{1-x}\text{Ir}_x\text{Cl}_3$  ( $x$  values indicated in legend) single crystals with a magnetic field of  $B = 1$  T applied in the  $ab$  plane. Inset: magnification of low-temperature range. Red arrow and black/grey arrows mark the evolution of  $T_{N1}$  and  $T_{N2}$ , respectively. (b) Field-dependent magnetization at 2 K. Inset: Curie-Weiss intercepts  $T_{CW}$  for various compositions with a field of 2 T. (c) Heat capacity curves of low-doped crystals. Solid lines are an estimate of the lattice contribution. Dashed lines are a guide to the eye.

only when the 2D percolation threshold is crossed.

Single crystals of  $\text{Ru}_{1-x}\text{Ir}_x\text{Cl}_3$  were prepared using vapor transport techniques from commercial powders of  $\alpha\text{-RuCl}_3$  and  $\alpha\text{-IrCl}_3$ . Polycrystalline  $\text{Ru}_{1-x}\text{Ir}_x\text{Cl}_3$  was also synthesized from direct reaction of the starting materials. The composition of each crystal was checked by energy dispersive x-ray spectroscopy, and  $x$  hereafter refers to the observed value averaged over a number of sites. Sin-

gle crystal X-ray diffraction experiments confirm a monoclinic  $C2/m$  space group in small  $\text{Ru}_{1-x}\text{Ir}_x\text{Cl}_3$  crystals consistent with the end members,  $\alpha\text{-RuCl}_3$  and  $\alpha\text{-IrCl}_3$  [63], with Ir substituting for Ru on the  $4g$  site. In line with previous studies [13, 34] we adopt trigonal notation in the following discussion for simplicity; this affords a more natural representation of the honeycomb planes and, in fact, properly describes the room temperature structure of many larger ( $> 1\text{mm}$  diameter)  $\alpha\text{-RuCl}_3$  crystals [64]. Single crystal neutron diffraction ( $[H\ 0\ L]$  scattering plane) and HB-3A four-circle diffractometer at the High Flux Isotope Reactor at ORNL with incident neutron wavelengths of 2.36 and 1.546 Å, respectively. Muon spin rotation experiments on powder samples were performed at the TRIUMF M20 beamline in the LAMPF  $\mu\text{SR}$  spectrometer.

Figure 1(a) shows the in-plane magnetic susceptibility of a series of  $\text{Ru}_{1-x}\text{Ir}_x\text{Cl}_3$  single crystals. In addition to the  $T_{N1} = 7$  K zig-zag transition of the parent compound, a second feature at  $T_{N2} \leq 14$  K for  $x > 0$  (black arrow, Fig.1a Inset) indicates that doped crystals obtained from the current growth process are not completely free of stacking faults. The sharp cusp in the susceptibility at  $T_{N1}$  is rapidly shifted toward lower temperatures at non-zero  $x$  (red arrow) denoting a global suppression of the ordering temperatures with dilution. As doping increases, the minority phase contribution ( $T_{N2}$ ) becomes more visible and is the only transition evident above 2 K by  $x = 0.09$ . Further Ir substitution leads to a rounding of the cusp at  $T_{N2}$  (grey arrow), which decreases continuously with  $x$  and disappears at the percolation limit of the honeycomb lattice,  $x \sim 0.3$  [65]. Strong irreversibility between zero-field-cooled and field-cooled curves was not observed at any level of site dilution, in notable contrast to the spin-glass-like characteristics reported in the honeycomb iridates with non-magnetic substitution [61].

The low-temperature susceptibility does not decrease monotonically with  $x$ , but shows an increase for  $0.07 < x < 0.16$ . The origin of this behavior is unexplained, however it is interesting to note that vacancies in a site diluted Kitaev model have been shown to lead to an increase in the local susceptibility [52, 53, 57].

Large effective paramagnetic moments of the  $S = 1/2$  Ru ions in  $\alpha\text{-RuCl}_3$  have been previously noted and are attributed to a mixed spin-orbital character [66]. For  $\text{Ru}_{1-x}\text{Ir}_x\text{Cl}_3$  the effective paramagnetic moment per formula unit determined from Curie-Weiss fittings of the high-temperature data decreased from  $2.4 \mu_B$  at  $x = 0$  to  $1.9 \mu_B$  at  $x = 0.30$ , consistent with  $S = 0$  Ir ions within systematic uncertainties. Normalized to Ru content, the moment per Ru ion in  $\text{Ru}_{1-x}\text{Ir}_x\text{Cl}_3$  retains large values in the range of  $2.3 - 2.7 \mu_B/\text{Ru}^{3+}$ ; a significant trend with  $x$  cannot be established from the current experiment, however some small systematic dependence also cannot be ruled out. Curie-Weiss intercepts  $T_{CW}$  (Inset, Fig. 2b) are positive in all samples and follow an

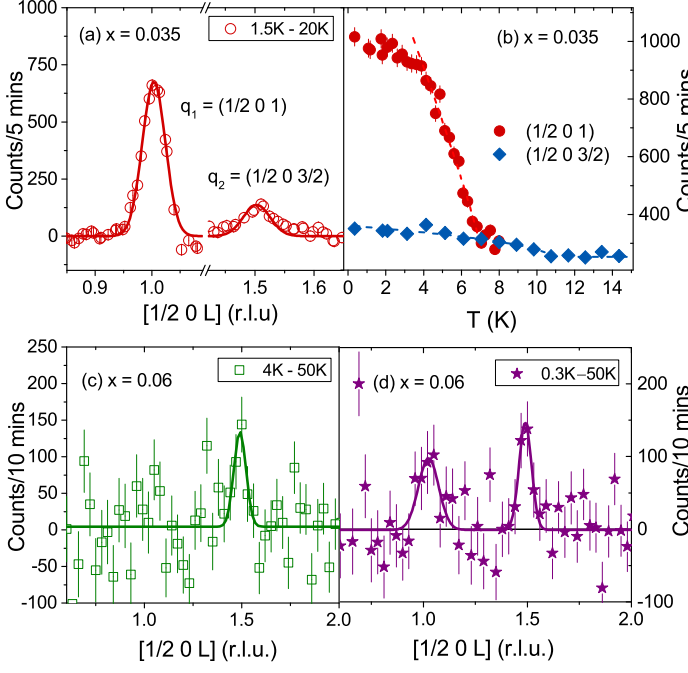


FIG. 2. (a) Wavevector scan at 1.5K collected at HB-1A along  $[1/2\ 0\ L]$  through characteristic magnetic reflections  $\mathbf{q}_1 = (1/2\ 0\ 1)$  and  $\mathbf{q}_2 = (1/2\ 0\ 3/2)$  for a 50 mg single crystal with  $x = 0.035$ . 20 K ( $T > T_N$ ) data are subtracted as a background. (b) Temperature scans of the scattering intensity at  $\mathbf{q}_1$  and  $\mathbf{q}_2$ . Wavevector scans along  $[1/2\ 0\ L]$  at (c) 4 K and (d) 0.3 K in a 20 mg single crystal with  $x = 0.06$ . 50 K data are subtracted as a background.

overall decreasing trend with doping, although the values appear to level off at  $T_{CW} \sim 20\text{K}$  for  $x > 0.1$  after initially dropping more rapidly. In the parent compound the field-dependent magnetization at 2 K shows an upward curvature approaching a crossover out of the zig-zag phase near 8 T [14, 20]. For  $x > 0.09$ , the field-dependent magnetization curves in Fig. 2(b) develop opposite concavity from the clean limit. Interestingly, this coincides with the region of increase in the low temperature susceptibility mentioned above. The turnover in the magnetization curves at large  $x$  is not captured by a simple Brillouin function for free or nearly free spins.

Anomalies in the specific heat at  $T_{N1}$  and  $T_{N2}$  mirror the downward trend with doping observed in susceptibility measurements (Fig. 1c). Away from the transition points all curves can be described by  $C_p \propto T^2$ , an approximation of the 2D Debye law characteristic of other van der Waals bonded materials [67]. The 2D character of the materials is thus not strongly affected by Ir substitution. Weak low temperature features with a magnetic origin (indicated by magnetic field dependence) are observed at larger  $x$  of 0.2 and 0.3, however, the absence of a  $\lambda$ -like anomaly is not consistent with a long-range ordering transition above 2 K (see supplementary information [SI]).

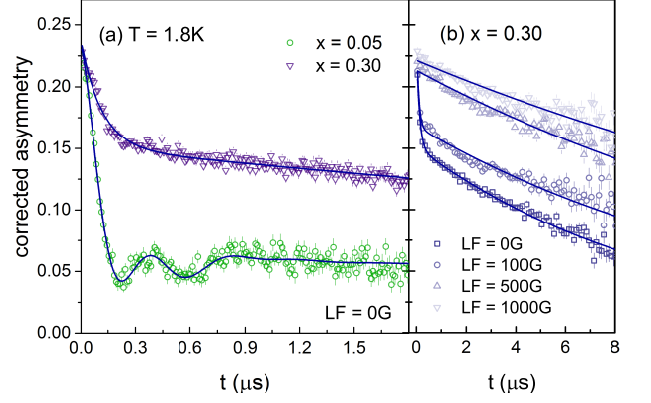


FIG. 3. (a) Zero-field  $\mu\text{SR}$  spectra for  $\text{Ru}_{1-x}\text{Ir}_x\text{Cl}_3$  ( $x = 0.05, 0.30$ ) powders. Solid lines are a fit to a two-component relaxation of the form  $A_i e^{-\lambda_i t} \cos(\omega_i t)$  ( $x = 0.05$ ) and  $A_i e^{-\lambda_i t}$  ( $x = 0.3$ ). (b) Longitudinal field curves for  $x = 0.30$  at 1.8 K show a decoupling of the fast component in  $\text{LF} \geq 500$  G with persisting exponential relaxation due to spin fluctuations.

The magnetic ground state of lightly-doped crystals with  $x \leq 0.06$  was characterized in neutron diffraction experiments. As in the undoped system with stacking faults [13, 34] we observe two magnetic propagation vectors  $\mathbf{q}_1 = (1/2\ 0\ 1)$  and  $\mathbf{q}_2 = (1/2\ 0\ 3/2)$ , corresponding to zig-zag order with ABC and ABAB magnetic layer stacking, respectively, in Ir-substituted single crystals measured at HB-1A (Fig. 2). For  $x = 0.035$  the relative peak intensities  $I(\mathbf{q}_1)/I(\mathbf{q}_2) \sim 6$  at 1.5 K show that the majority of the sample adopts the ABC-type structure. The onset of scattering intensity at  $\mathbf{q}_1$  is spread over several Kelvin compared to the parent compound, which could indicate distribution in  $T_{N1}$  related to compositional variation [SI]. The center of the transition at  $\sim 5.5$  K is consistent with the location of features in  $\chi$  and  $C_p$  for similarly doped samples. An extensive survey of reciprocal space using the four-circle diffractometer did not reveal additional peaks associated with alternative magnetically ordered states in the H-K- $\Gamma$  phase diagram. An ordered moment of  $0.32(2)\ \mu_B$  in the modulated ABC zig-zag phase was determined after collecting a large set of nuclear reflections to yield the scale factor for normalization of the magnetic peak intensity, approximately two-thirds of the value in pure  $\alpha\text{-RuCl}_3$  [21, 68].

An increase in Ir-content from  $x = 0.035$  (Fig. 2a-b) to  $x = 0.06$  (Fig. 2c-d) strongly affected  $T_{N1}$  as well as the relative amount of the two magnetic phases. Scans along  $(1/2\ 0\ L)$  show a single peak at  $L = 3/2$  at 4 K (Fig. 2c). A second peak at  $L = 1$  was resolved only in lower temperature scans at 1.6 K and 0.3 K. The intensity of the peak at  $\mathbf{q}_1$  dropped precipitously with respect to  $\mathbf{q}_2$ , yielding  $I(\mathbf{q}_1)/I(\mathbf{q}_2) \sim 0.7$  at the experimental base temperature of 0.3 K (Fig. 2d). No additional peaks were observed at wavevectors characteristic of other candidate magnetic structures that could be accessed in the  $(H\ 0\ L)$  scattering plane. It is thus unlikely that a dis-

ting magnetic order phase arises as the ABC-type zig-zag order is suppressed in the dilute system. The temperature dependence of the scattering at  $\mathbf{q}_2$  yielded  $T_{N2} = 10.2(2)$  K and  $10.0(9)$  K for  $x = 0.035$  and  $0.06$ , respectively. The relatively slower decline of  $T_{N2}$  with Ir content compared to  $T_{N1}$  is consistent with the bulk measurements in Fig. 1.

$\mu$ SR measurements were performed on  $\text{Ru}_{1-x}\text{Ir}_x\text{Cl}_3$  powders to characterize the weakly magnetic state of the dilute system. Polycrystalline  $\text{RuCl}_3$  undergoes a single broad transition at 14 K with ABAB magnetic structure [21]; Ir-substituted powders also exhibit a single transition of the ABAB type that disappears near the percolation limit [SI]. The relaxation of the muon asymmetry  $a(t)$  reflects the amplitudes and fluctuations of local magnetic fields [69].  $\mu$ SR spectra of  $\text{Ru}_{1-x}\text{Ir}_x\text{Cl}_3$  with  $x = 0.05$  show only nuclear contributions to the relaxation at 20 K. A fast-relaxing component emerges below  $T_N$  and well-defined oscillations signifying long-range magnetic order develop by 1.8 K (Fig. 3a). Two distinct frequencies  $\omega_1/2\pi \sim 2.5$  MHz and  $\omega_2/2\pi \sim 1$  MHz are observed, in agreement with a recent report in  $\alpha$ - $\text{RuCl}_3$  powders that found two inequivalent muon sites in the pseudo-bilayer zig-zag phase [70].

In contrast, at  $x = 0.30$  no coherent muon precession frequencies that would indicate long-range order are resolved at any temperature down to 1.8 K. The 1.8 K spectrum is comprised instead of exponential terms  $A_i e^{-\lambda_i t}$ , consistent with the fast-fluctuation limit of distributed internal magnetic fields [69]. Longitudinal field experiments, in which spin depolarization due to static internal fields is suppressed, (Fig. 3b) were used to distinguish between static and dynamic processes in the  $x = 0.30$  sample. A static origin can be assigned to the early rapid depolarization in the zero-field spectrum ( $\lambda_1 \sim 9$  MHz), which is decoupled in a longitudinal field  $\text{LF} \geq 500$  G (Fig. 3b). However, the persistence of the slow exponential decay term  $\lambda_2 \sim 0.1$  MHz in the LF spectra is a clear demonstration of dynamic magnetism in the fast-fluctuation limit in the remaining volume of the sample. It is unknown whether or not these two components are also present in the single crystals.

The phase diagram of  $\text{Ru}_{1-x}\text{Ir}_x\text{Cl}_3$  determined from the current study is summarized in Figure 4. The Neel temperatures of both ABC and ABAB stacked phases are universally decreased by incorporation of nonmagnetic  $\text{Ir}^{3+}$ . Linear fits to the normalized critical temperatures give initial suppression rates [71]  $-d[T_{Ni}/T_{Ni}(0)]/dx = 8.1(7)$  for  $T_{N1}$  and  $4.4(3)$  for  $T_{N2}$ . The more sensitive response to magnetic site dilution in the ABC phase is likely related to a higher degree of frustration in magnetic interactions for 3-layer magnetic stacking than for 2-layer stacking. This disparity is evident in the different  $T_N$  values for the two phases in the parent compound. Extrapolating linearly from small  $x$ , the suppression of the zig-zag phase with ABC periodicity to  $T = 0$  occurs for  $x \sim 0.11$ , with  $x \sim 0.22$  for ABAB-type. For the

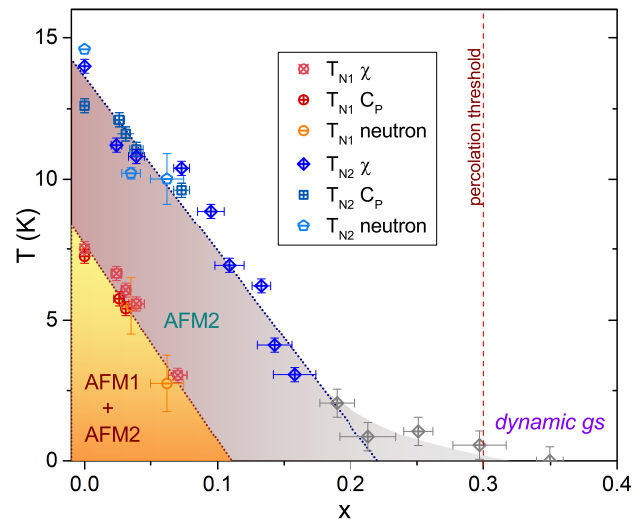


FIG. 4. Phase diagram of  $\text{Ru}_{1-x}\text{Ir}_x\text{Cl}_3$ . Transition temperatures  $T_{N1}$  (red symbols) and  $T_{N2}$  (blue symbols) determined from magnetic susceptibility, heat capacity, and neutron diffraction mark the boundaries of the ABC-stacked (AFM1) and ABAB-stacked (AFM2) zig-zag phases in regions of pristine monoclinic structure and a high degree of stacking faults, respectively. Linear fitting to  $T_N(x)$  (dashed lines) gives a critical dilution level for  $T_{N1} \rightarrow 0$  of  $x \sim 0.11$ . The cusp at  $T_{N2}$  is driven below the experimental base temperature of 2 K by  $x \sim 0.2$ ; at larger  $x$   $T_{N2}$  is estimated by extrapolation to  $d\chi/dT = 0$  (grey symbols).  $\mu$ SR measurements indicate a dynamic ground state in polycrystalline samples at  $x = 0.3$  with rapidly fluctuating internal fields.

latter magnetic correlations fall off more slowly at large  $x$  and persist until the percolation threshold of the 2D honeycomb lattice is crossed. A polycrystalline sample at this dilution level ( $x = 0.3$ ) exhibited fast magnetic fluctuations in  $\mu$ SR measurements. Future careful experiments at lower temperatures near the critical dilution will show if the extinction of the long-range order reveals any critical behavior.

This phase diagram illustrates one method for suppressing magnetic order in a system exhibiting Kitaev physics, and shows a possible avenue for approaching the QSL phase. Suggestive indications including the unusual behavior of the susceptibility with doping and the persistent dynamics at the percolation threshold merit further experimental and theoretical attention. In particular, detailed low temperature spectroscopic investigations are called for to determine whether or not QSL physics is present.

### Acknowledgments

P.L.K and D.M. were supported by the Gordon and Betty Moore Foundations EPiQS Initiative through Grant GBMF4416. J.-Q.Y. acknowledges support from the U.S. Department of Energy, Office of Science, Office of Basic Energy Sciences, Materials Sciences and Engineering Division. The work at ORNL HFIR was sponsored by the Scientific User Facilities Division, Office

of Basic Energy Sciences, U.S. Department of Energy. We thank Iain McKenzie for local support at TRIUMF, Bryan Chakoumakos and Feng Ye for assistance with single-crystal XRD, and Brian Sales, Michael McGuire, and Andrew May for helpful discussions during the course of this research.

- 
- [1] L. Balents, *Nature* **464**, 199 (2010).
  - [2] L. Savary and L. Balents, arXiv:1601.03742.
  - [3] C. Nayak, S. H. Simon, A. Stern, M. Freedman, and S. Das Sarma, *Rev. Mod. Phys.* **80**, 1083 (2008).
  - [4] A. Y. Kitaev, *Annals of Physics* **303**, 2 (2003).
  - [5] A. Kitaev, *Annals of Physics* **321**, 2 (2006).
  - [6] G. Jackeli and G. Khaliullin, *Phys. Rev. Lett.* **102**, 017205 (2009).
  - [7] Y. Singh and P. Gegenwart, *Phys. Rev. B* **82**, 064412 (2010).
  - [8] Y. Singh, S. Manni, J. Reuther, T. Berlijn, R. Thomale, W. Ku, S. Trebst, and P. Gegenwart, *Phys. Rev. Lett.* **108**, 127203 (2012).
  - [9] S. Hwan Chun, J.-W. Kim, J. Kim, H. Zheng, C. C. Stoumpos, C. D. Malliakas, J. F. Mitchell, K. Mehlawat, Y. Singh, Y. Choi, T. Gog, A. Al-Zein, M. M. Sala, M. Krisch, J. Chaloupka, G. Jackeli, G. Khaliullin, and B. J. Kim, *Nat Phys* **11**, 462 (2015).
  - [10] J. Chaloupka and G. Khaliullin, *Phys. Rev. B* **94**, 064435 (2016).
  - [11] K. W. Plumb, J. P. Clancy, L. J. Sandilands, V. V. Shankar, Y. F. Hu, K. S. Burch, H.-Y. Kee, and Y.-J. Kim, *Phys. Rev. B* **90**, 041112 (2014).
  - [12] H.-S. Kim, V. S. V., A. Catuneanu, and H.-Y. Kee, *Phys. Rev. B* **91**, 241110 (2015).
  - [13] A. Banerjee, C. A. Bridges, J.-Q. Yan, A. A. Aczel, L. Li, M. B. Stone, G. E. Granroth, M. D. Lumsden, Y. Yiu, J. Knolle, S. Bhattacharjee, D. L. Kovrizhin, R. Moessner, D. A. Tennant, D. G. Mandrus, and S. E. Nagler, *Nat. Mater.* **15**, 733 (2016).
  - [14] Y. Kubota, H. Tanaka, T. Ono, Y. Narumi, and K. Kindo, *Phys. Rev. B* **91**, 094422 (2015).
  - [15] X. Liu, T. Berlijn, W.-G. Yin, W. Ku, A. Tsvelik, Y.-J. Kim, H. Gretarsson, Y. Singh, P. Gegenwart, and J. P. Hill, *Phys. Rev. B* **83**, 220403 (2011).
  - [16] F. Ye, S. Chi, H. Cao, B. C. Chakoumakos, J. A. Fernandez-Baca, R. Custelcean, T. F. Qi, O. B. Korneta, and G. Cao, *Phys. Rev. B* **85**, 180403 (2012).
  - [17] S. K. Choi, R. Coldea, A. N. Kolmogorov, T. Lancaster, I. I. Mazin, S. J. Blundell, P. G. Radaelli, Y. Singh, P. Gegenwart, K. R. Choi, S.-W. Cheong, P. J. Baker, C. Stock, and J. Taylor, *Phys. Rev. Lett.* **108**, 127204 (2012).
  - [18] S. C. Williams, R. D. Johnson, F. Freund, S. Choi, A. Jesche, I. Kimchi, S. Manni, A. Bombardi, P. Manuel, P. Gegenwart, and R. Coldea, *Phys. Rev. B* **93**, 195158 (2016).
  - [19] J. A. Sears, M. Songvilay, K. W. Plumb, J. P. Clancy, Y. Qiu, Y. Zhao, D. Parshall, and Y.-J. Kim, *Phys. Rev. B* **91**, 144420 (2015).
  - [20] R. D. Johnson, S. C. Williams, A. A. Haghighirad, J. Singleton, V. Zapf, P. Manuel, I. I. Mazin, Y. Li, H. O. Jeschke, R. Valenti, and R. Coldea, *Phys. Rev. B* **92**, 235119 (2015).
  - [21] H. B. Cao, A. Banerjee, J.-Q. Yan, C. A. Bridges, M. D. Lumsden, D. G. Mandrus, D. A. Tennant, B. C. Chakoumakos, and S. E. Nagler, *Phys. Rev. B* **93**, 134423 (2016).
  - [22] J. G. Rau, E. K.-H. Lee, and H.-Y. Kee, *Phys. Rev. Lett.* **112**, 077204 (2014).
  - [23] J. Reuther, R. Thomale, and S. Rachel, *Phys. Rev. B* **90**, 100405 (2014).
  - [24] J. Chaloupka, G. Jackeli, and G. Khaliullin, *Phys. Rev. Lett.* **110**, 097204 (2013).
  - [25] J. Chaloupka and G. Khaliullin, *Phys. Rev. B* **92**, 024413 (2015).
  - [26] J. Chaloupka, G. Jackeli, and G. Khaliullin, *Phys. Rev. Lett.* **105**, 027204 (2010).
  - [27] Y. Sizyuk, C. Price, P. Wölfle, and N. B. Perkins, *Phys. Rev. B* **90**, 155126 (2014).
  - [28] Y. Sizyuk, P. Wölfle, and N. B. Perkins, *Phys. Rev. B* **94**, 085109 (2016).
  - [29] R. Yadav, N. A. Bogdanov, V. M. Katukuri, S. Nishimoto, J. v. d. Brink, and L. Hozoi, *Sci. Rep.* **6**, 37925 (2016).
  - [30] V. M. Katukuri, S. Nishimoto, V. Yushankhai, A. Stoyanova, H. Kandpal, S. Choi, R. Coldea, I. Rousochatzakis, L. Hozoi, and J. v. d. Brink, *New J. Phys.* **16**, 013056 (2014).
  - [31] K. Foyevtsova, H. O. Jeschke, I. I. Mazin, D. I. Khomskii, and R. Valenti, *Phys. Rev. B* **88**, 035107 (2013).
  - [32] S. M. Winter, Y. Li, H. O. Jeschke, and R. Valenti, *Phys. Rev. B* **93**, 214431 (2016).
  - [33] K. Shinjo, S. Sota, and T. Tohyama, *Phys. Rev. B* **91**, 054401 (2015).
  - [34] A. Banerjee, J.-Q. Yan, J. Knolle, C. A. Bridges, M. B. Stone, M. D. Lumsden, D. G. Mandrus, D. A. Tennant, R. Moessner, and S. E. Nagler, arXiv:1609.00103 (2016).
  - [35] L. J. Sandilands, Y. Tian, K. W. Plumb, Y.-J. Kim, and K. S. Burch, *Phys. Rev. Lett.* **114**, 147201 (2015).
  - [36] J. Nasu, J. Knolle, D. L. Kovrizhin, Y. Motome, and R. Moessner, *Nat. Phys.* **12**, 912 (2016).
  - [37] S. Nath Gupta, P. V. Sriluckshmy, K. Mehlawat, A. Balodhi, D. K. Mishra, S. R. Hassan, T. V. Ramakrishnan, D. V. S. Muthu, Y. Singh, and A. K. Sood, *Europhys. Lett.* **114**, 47004 (2016).
  - [38] J. Knolle, D. Kovrizhin, J. Chalker, and R. Moessner, *Phys. Rev. Lett.* **112**, 207203 (2014).
  - [39] J. Knolle, G.-W. Chern, D. Kovrizhin, R. Moessner, and N. Perkins, *Phys. Rev. Lett.* **113**, 187201 (2014).
  - [40] B. Perreault, J. Knolle, N. B. Perkins, and F. J. Burnell, *Phys. Rev. B* **94**, 104427 (2016).
  - [41] T. Hyart, A. R. Wright, G. Khaliullin, and B. Rosenow, *Phys. Rev. B* **85**, 140510(R) (2012).
  - [42] Y.-Z. You, I. Kimchi, and A. Vishwanath, *Phys. Rev. B* **86**, 085145 (2012).
  - [43] J.-W. Mei, *Phys. Rev. Lett.* **108**, 227207 (2012).
  - [44] S. Okamoto, *Phys. Rev. Lett.* **110**, 066403 (2013).
  - [45] S. Okamoto, *Phys. Rev. B* **87**, 064508 (2013).
  - [46] F. Trouselet, P. Horsch, A. M. Ole, and W.-L. You, *Phys. Rev. B* **90**, 024404 (2014).
  - [47] L. Kimme, T. Hyart, and B. Rosenow, *Phys. Rev. B* **91**, 220501(R) (2015).
  - [48] G. B. Halasz, J. T. Chalker, and R. Moessner, *Phys. Rev. B* **90**, 035145 (2014).
  - [49] F. Zschöcke and M. Vojta, *Phys. Rev. B* **92**, 014403 (2015).
  - [50] J. Brennan and J. Vala, *J. Phys. Chem. A* **120**, 3326 (2016).

- [51] K. Dhochak, R. Shankar, and V. Tripathi, Phys. Rev. Lett. **105** (2010).
- [52] A. J. Willans, J. T. Chalker, and R. Moessner, Phys. Rev. Lett. **104**, 237203 (2010).
- [53] A. J. Willans, J. T. Chalker, and R. Moessner, Phys. Rev. B **84**, 115146 (2011).
- [54] S. G., V. Sreenath, A. Lakshminarayan, and R. Narayanan, Phys. Rev. B **85**, 054204 (2012).
- [55] E. C. Andrade and M. Vojta, Phys. Rev. B **90**, 205112 (2014).
- [56] G. J. Sreejith, S. Bhattacharjee, and R. Moessner, Phys. Rev. B **93**, 064433 (2016).
- [57] F. Trouselet, G. Khaliullin, and P. Horsch, Phys. Rev. B **84**, 054409 (2011).
- [58] K. Mehlawat, G. Sharma, and Y. Singh, Phys. Rev. B **92**, 134412 (2015).
- [59] S. Manni, Y. Tokiwa, and P. Gegenwart, Phys. Rev. B **89**, 241102(R) (2014).
- [60] G. Cao, T. F. Qi, L. Li, J. Terzic, V. S. Cao, S. J. Yuan, M. Tovar, G. Murthy, and R. K. Kaul, Phys. Rev. B **88** (2013).
- [61] S. Manni, S. Choi, I. I. Mazin, R. Coldea, M. Altmeyer, H. O. Jeschke, R. Valenti, and P. Gegenwart, Phys. Rev. B **89**, 245113 (2014).
- [62] K. Rolfs, S. Toth, E. Pomjakushina, D. Sheptyakov, J. Taylor, and K. Conder, Phys. Rev. B **91**, 180406(R) (2015).
- [63] K. Brodersen, F. Moers, and H. Schnering, Naturwissenschaften **52**, 205 (1965).
- [64] M. Ziatdinov, A. Banerjee, A. Maksov, T. Berlijn, W. Zhou, H. Cao, J.-Q. Yan, C. A. Bridges, D. G. Mandrus, S. E. Nagler, A. P. Baddorf, and S. V. Kalinin, Nature Comm. **7**, 13774 (2016).
- [65] X. Feng, Y. Deng, and H. W. J. Blote, Phys. Rev. E **78**, 031136 (2008).
- [66] M. Majumder, M. Schmidt, H. Rosner, A. A. Tsirlin, H. Yasuoka, and M. Baenitz, Phys. Rev. B **91**, 180401 (2015).
- [67] J. Krumhansl and H. Brooks, J. Chem. Phys. **21**, 1663 (1953).
- [68] Two scenarios have been proposed for the magnetic structure of  $\text{RuCl}_3$  perpendicular to the honeycomb layers - modulation of the moment size or a 120 degree spiral. In  $\text{Ru}_{1-x}\text{Ir}_x\text{Cl}_3$  with  $x = 0.035$  these models yield 0.32(2) and 0.27(2)  $\mu_B$  per formula unit, respectively. As in the parent compound, the modulated structure provides a slightly better fit to the data.
- [69] P. D. d. Rotier and A. Yaouanc, J. Phys.: Condens. Matter **9**, 9113 (1997).
- [70] F. Lang, P. J. Baker, A. A. Haghighirad, Y. Li, D. Prabhakaran, R. Valenti, and S. J. Blundell, Phys. Rev. B **94**, 020407 (2016).
- [71] S.-W. Cheong, A. S. Cooper, L. W. Rupp, B. Batlogg, J. D. Thompson, and Z. Fisk, Phys. Rev. B **44**, 9739 (1991).



## SUPPLEMENTARY INFORMATION

### I. SAMPLE PREPARATION AND STRUCTURE

Single crystals of  $\text{Ru}_{1-x}\text{Ir}_x\text{Cl}_3$  were grown by a transport method at high temperatures (900-1100°C) from commercial powders of  $\text{RuCl}_3$  (Furuya Metals) and  $\text{IrCl}_3$  (American Elements) in the presence of  $\text{NaCl}$ . Single crystal diffraction (Rigaku,  $\text{Mo K}\alpha$  radiation) was performed for the compositions  $x = 0.05$  and  $x = 0.15$  on small crystals with  $\sim 100\mu\text{m}$  in-plane dimension. The structure was refined using SHELX to the monoclinic  $\text{C2/m}$  space group, consistent with similarly-sized  $\text{RuCl}_3$  single crystals. Individual planes of the larger ( $\sim\text{mm}$ ) sized plate-like crystals used in SQUID and heat capacity measurements were checked by X-ray diffraction on a Panalytical Xpert Pro powder diffractometer. Indexed in the trigonal  $\text{P3}_112$  setting, the out-of-plane lattice parameter of these crystals as determined from the (0 0 L) peaks decreases linearly with increasing Ir substitution (Fig. S1a).  $\text{Ru}_{1-x}\text{Ir}_x\text{Cl}_3$  was prepared by direct reaction of the commercial starting materials in an evacuated quartz ampoule at 800°C. XRD patterns (Fig. S1b) show strong (0 0 L) texturing in a fraction of the powder samples, and Warren lineshapes are characteristic of the quasi-2D nature of the system. Minority oxide and binary metal phases ( $< 5$  wt. %) identified in the powder patterns likely indicate a partial decomposition of the starting materials on heating. The c-axis lattice parameters determined from XRD are in good agreement with those of the single crystal samples while the in-plane lattice parameter grows systematically with incorporation of Ir (Fig. S1a).

### II. COMPOSITION

The elemental compositions of the  $\text{Ru}_{1-x}\text{Ir}_x\text{Cl}_3$  single in this study were checked by energy dispersive X-ray spectroscopy (EDS). Variation of Ru/Ir ratio over  $\sim\text{mm}$  length scales was noted in samples large enough for bulk measurements; the distribution of  $x$  was characterized in each sample by measuring a large number of sites spanning the crystal with a spot size of 20–30 $\mu\text{m}$ . Representative histograms for twelve crystals are shown in Fig. S2. Standard deviation from the mean value of  $x$  ranged from 0.3 mol % Ir to 2 mol% Ir, but remained less than 1% in nearly all of  $>20$  samples tested.

### III. MAGNETIC TRANSITION TEMPERATURES

Magnetic transition temperatures were estimated either from the cusp ( $\frac{d\chi}{dT} = 0$ ) in the temperature-dependent susceptibility curves or by linear extrapolation of data above and below the turnover in  $\chi$  where  $T_{N2}$  appears as a

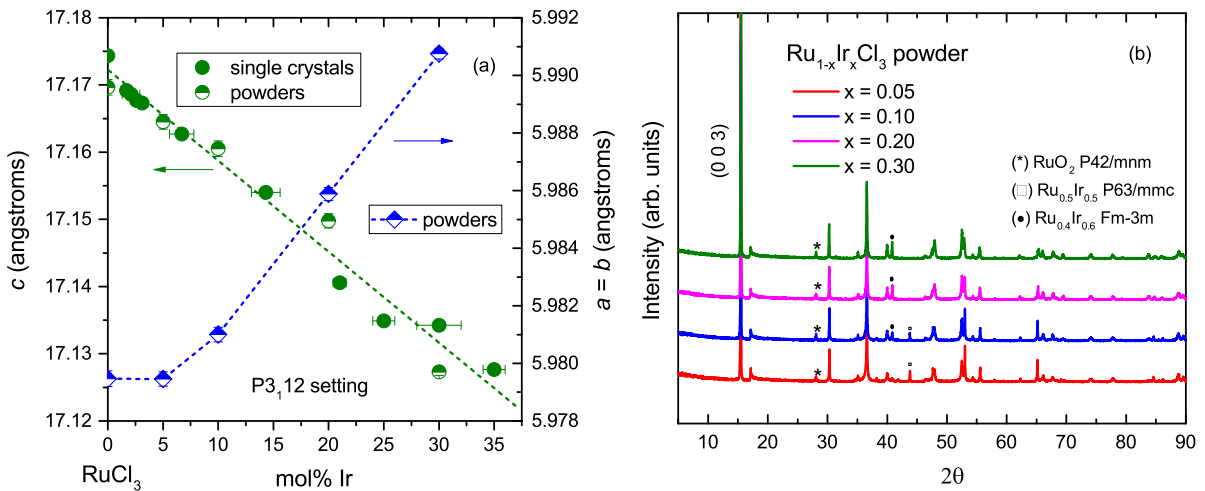


FIG. S1. Fig. S1 (a) Room temperature lattice parameters of  $\text{Ru}_{1-x}\text{Ir}_x\text{Cl}_3$  single crystals (filled symbols) and powders (half-filled symbols) in the trigonal setting. Lines are a guide to the eye. (b) Offset X-ray diffraction patterns of  $\text{Ru}_{1-x}\text{Ir}_x\text{Cl}_3$  powders. Average Ir content and distribution is determined by EDS measurements in single crystals; Ir doping in the powdered materials is taken as the nominal value.



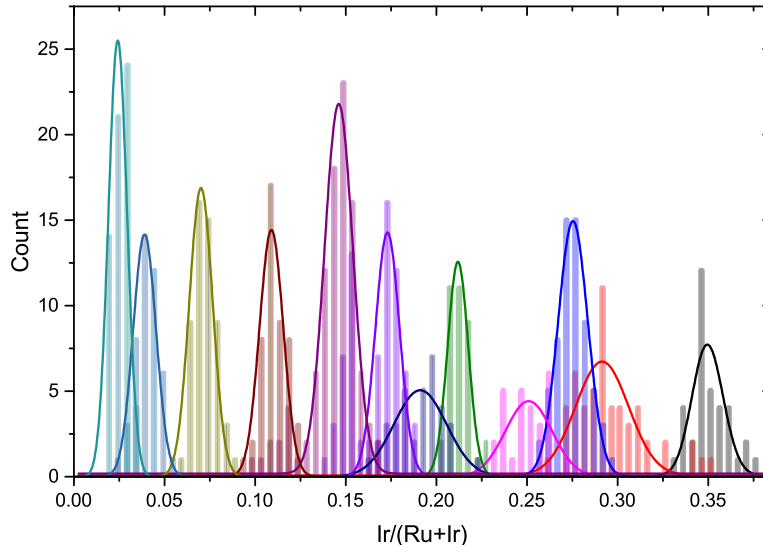


FIG. S2. Histograms representing the substitution level  $\text{Ir}/(\text{Ru}+\text{Ir})$  over a number of sites in single crystals of  $\text{Ru}_{1-x}\text{Ir}_x\text{Cl}_3$  as determined by EDS measurements. Solid lines represent a Gaussian fit to the distribution in each sample.

shoulder no well-defined cusp exists (e.g.  $T_{N2}$  in 2-phase samples or large  $x$ ), as in Fig. S3(a-b). Critical temperatures determined in this way are in good agreement with heat capacity and neutron diffraction measured in select samples (Fig. S3c-f).

#### IV. HYSTERESIS

To check for the presence of spin-glass-like freezing and/or thermal hysteresis at low temperatures, susceptibility was measured in a magnetic field of 1 T under zero-field-cooled (ZFC), field-cooled cooling (FCC) and field-cooled warming (FCW) protocols for several compositions spanning the range investigated. No splitting was observed between the ZFC/FC curves in Fig. S4(a) or in FCC/FCW curves (not shown) at this field that would indicate frozen moments or a strongly first-order phase transition, respectively.

#### V. MAGNETIC PHASES

The presence of two magnetic phases in  $\text{RuCl}_3$  is closely tied to structural details (see discussion in [1]) and thus their volume fraction can be expected to vary sensitively with stacking faults, strain, etc. In general we observe both magnetic transitions in  $\text{Ru}_{1-x}\text{Ir}_x\text{Cl}_3$  crystals, however the relative prominence of  $T_{N1}$  and  $T_{N2}$  transitions in heat capacity and susceptibility (Fig. S3) indicate that the volume fractions of these phases vary from one sample to the next. Fig. S4(b) shows susceptibility curves for three as-grown doped crystals from the same batch, qualitatively showing (i) dominant ABC phase, (ii) comparable contributions, and (iii) dominant ABAB phase. That similarly doped samples (i) and (iii) exhibit nearly single-phase ABC and ABAB characteristics, respectively, indicates that Ir-substitution does not necessarily lead to the ABAB-type phase (at least for low substitution levels  $x \leq 0.07$ ). Furthermore the proximity of  $T_{N1}$  and  $T_{N2}$  in the single and multiphase (ii) samples in Fig. S4(b) suggests that Ir is not segregated in regions with ABAB phase. The multiphase tendency in the doped crystals is thus most likely a result of the modified growth processes necessary to incorporate Ir in transported crystals.

#### VI. HEAT CAPACITY WITH $B \neq 0$

The anomalies at  $T_{N1}$  and  $T_{N2}$  in heat capacity curves were not affected by a magnetic field applied perpendicular to the  $ab$  plane (the only configuration available in our experimental setup) for small  $x$  (Fig. S5a-c), in agreement with

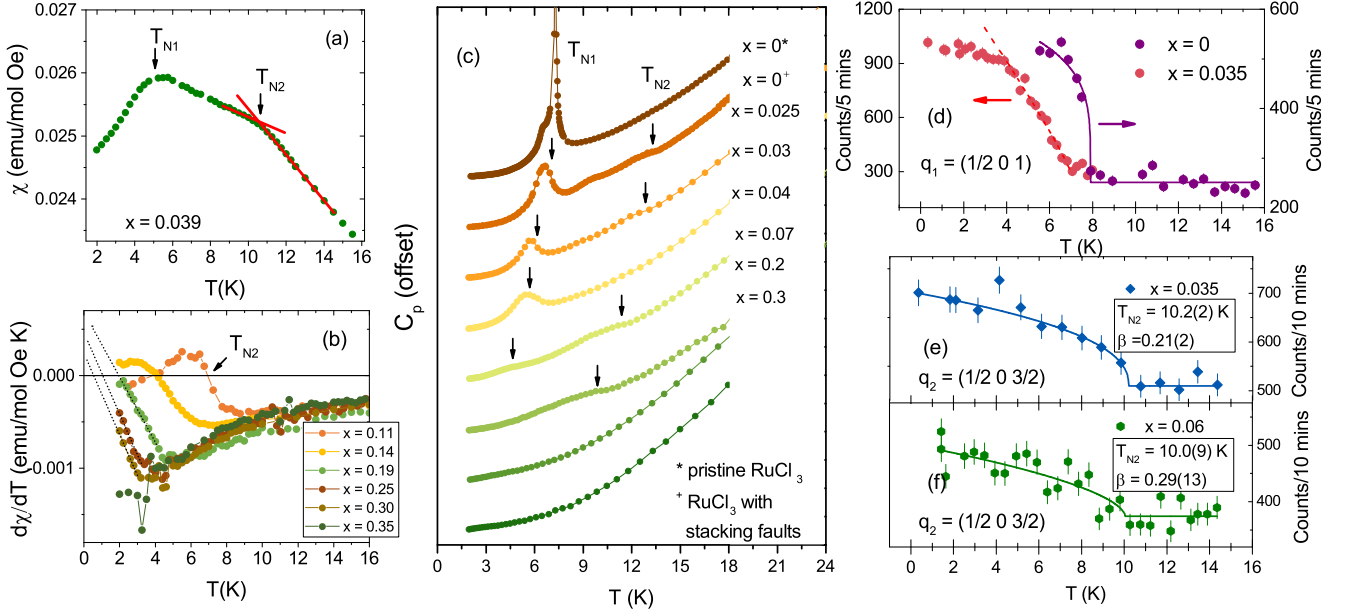


FIG. S3. Determination of magnetic transition temperatures (a),(b) from magnetic susceptibility curves. Solid lines in (b) represent linear extrapolation of  $d\chi/dT$  to estimate  $T_{N2}$  below the experimental base temperature of 2 K. (c) Offset heat capacity curves for various Ir substitution levels. Arrows indicate  $T_{N1}$  and  $T_{N2}$  (d) Intensity vs. temperature for the  $(1/2\ 0\ 1)$  magnetic Bragg peak showing  $T_{N1}$  in  $x = 0$  and  $x = 0.035(7)$  crystal. The doped crystal shows a smearing of the transition compared to the parent compound and intensity is not well described a power law. Dashed line is a guide to the eye. Solid line is a fit to  $I = I_0 + A(1 - \frac{T}{T_N})^{2\beta}$  for  $x = 0$ . (e),(f) Intensity vs. temperature for the  $(1/2\ 0\ 3/2)$  magnetic Bragg peak indicating  $T_{N2}$  for (e)  $x = 0.035(7)$  and (f)  $x = 0.062(13)$  single crystals. Solid lines are a power law fit.

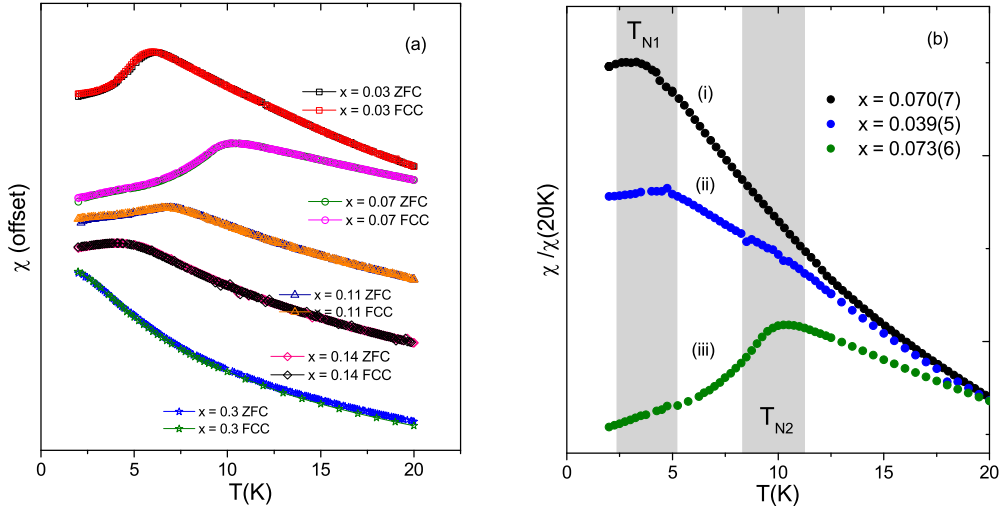


FIG. S4. (a) Susceptibility curves of  $\text{Ru}_{1-x}\text{Ir}_x\text{Cl}_3$  single crystals collected under zero-field-cooled warming (ZFC) and field-cooled cooling (FCC) protocols with a magnetic field of 1 T applied in plane. (b) Susceptibility curves, normalized to  $\chi(20\text{ K})$  for three Ir-doped crystals from the same batch indicating a variation of the ABC and ABAB magnetic phase fraction between samples, as characterized by the relative prominence of  $T_{N1}$  and  $T_{N2}$ .

a previous study on the parent compound, in which magnetic field dependence of the anomalies was only observed for  $B \parallel ab$  [2]. At large substitution levels  $x = 0.2$  and  $0.3$ , where susceptibility measurements indicate the magnetic transitions are suppressed below 2 K, an upturn is visible in  $C_p/T$  vs.  $T$  curves approaching the base temperature of 2 K (Fig. S6d-e), and  $C_p$  departs from a nearly  $T^2$  behavior below  $\sim 5$  K (Fig. S5f). Magnetic field partially suppresses this upturn (insets, Fig. S5), indicating that it has a magnetic origin. The feature may be related to short-range magnetic correlations, or represent the start of a very broad transition centered below 2 K. The emergence of field

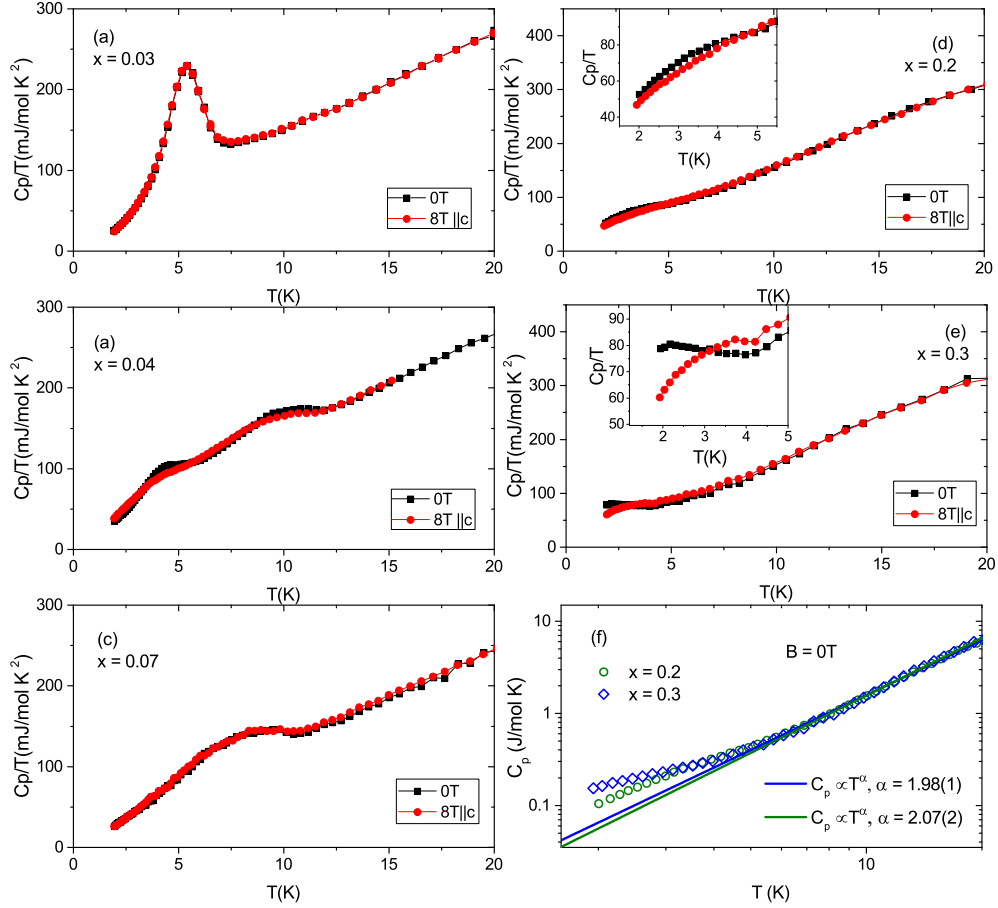


FIG. S5. Heat capacity curves  $C_p/T$  vs.  $T$  for in zero field and with an 8 T field applied perpendicular to the honeycomb plane in  $\text{Ru}_{1-x}\text{Ir}_x\text{Cl}_3$  crystals with (a)  $x = 0.03$ , (b)  $x = 0.04$ , (c)  $x = 0.07$ , (d)  $x = 0.2$ , and (e)  $x = 0.3$ . Insets are magnifications of the low-temperature region. (f)  $C_p$  vs.  $T$  for larger doping  $x = 0.2$  and  $x = 0.3$  showing a departure from  $C_p \propto T^2$  behavior below  $\sim 6$  K where curves exhibit field dependence.

dependence with  $B \parallel c$  points to a possible change in the magnetic anisotropies of the parent compound at large  $x$ , however a more detailed study with variation of the applied field direction in the crystals is required to explore this point.

## VII. FIELD-DEPENDENT MAGNETIZATION

Field-dependent magnetization curves for  $\text{Ru}_{1-x}\text{Ir}_x\text{Cl}_3$  single crystals at 2 K are shown in Fig. S6 over several doping ranges. Magnetization initially decreases with  $x$  up until  $\sim 10\%$  substitution and retains an upward curvature (Fig. S6a). In the range  $0.09 < x < 0.14$  magnetization increases and a switch in the concavity of  $M(H)$  occurs, with an approximately linear field dependence in the  $x = 0.11$  sample (Fig. S6b). At higher dopings,  $M(H)$  is concave down and magnetization decreases continuously (Fig. S6c).

We note that in the parent compound  $\text{RuCl}_3$ , field-dependent magnetization curves in the ordered state switch from concave up to concave down around  $H_C \sim 8$  T, shown in the inset of Fig. S6. The Ir-induced curvature change in the substituted samples could thus be explained by a downward shift in the critical field of the parent compound, with  $H_C \rightarrow 0$  for  $x \sim 0.11$ , or alternatively by additional contributions to the magnetization from vacancy-induced moments in the Kitaev framework.

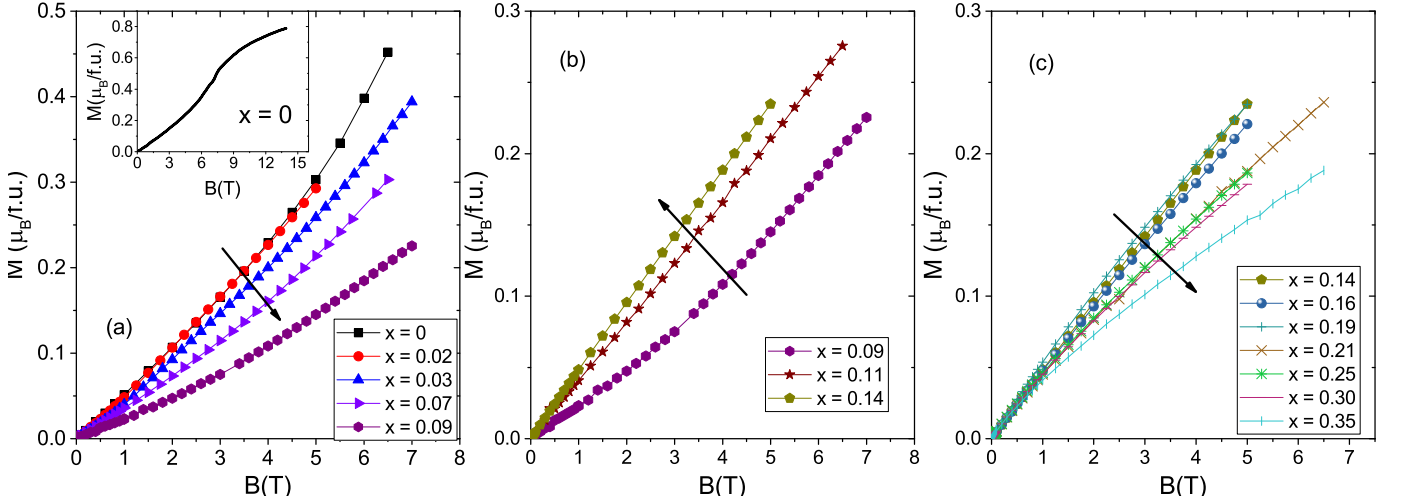


FIG. S6. Magnetization curves at 2 K with the magnetic field applied in-plane for Ru<sub>1-x</sub>Ir<sub>x</sub>Cl<sub>3</sub> crystals with (a)  $0 \leq x \leq 0.09$ , (b)  $0.09 \leq x \leq 0.14$ , and (c)  $0.14 \leq x \leq 0.35$ . Data were collected on two SQUID instruments with maximum magnetic fields of 5 T and 7 T. Inset: high-field dc magnetization curve for  $x = 0$  measured on a 14 T PPMS with an ACMS insert.

### VIII. MUON SPIN SPECTROSCOPY

Relaxation of the muon asymmetry due to nuclear moments in a polycrystalline sample is given by the well-known Kubo-Toyabe function,

$$a_{KT} = a_0 [1/3 + 2/3 (1 - \Delta^2 t^2) \exp(-\Delta^2 t^2)] \quad (1)$$

where  $\Delta$  is the width of the local distribution of static fields. At 20 K in the Ru<sub>1-x</sub>Ir<sub>x</sub>Cl<sub>3</sub> powders, weak Gaussian relaxation can be described by Eqn. 1, with  $\Delta = 0.093(1)$  and  $0.095(9) \mu\text{s}^{-2}$  for  $x = 0.05$  and  $x = 0.3$ , respectively. In the sample with  $x = 0.05$ , a fast-relaxing component emerges below  $T_N$  (see Fig. S8a) at 11 K and well-defined oscillations develop by 1.8 K. The asymmetry is generally modeled as

$$a(t) = a_0 [A_0 \exp(-\lambda_0 t) + \sum_{i=1,2} [A_i \exp(-\lambda_i t) \cos(2\pi\omega_i t)]] \quad (2)$$

where  $A_i$  represent the fast-relaxing/oscillating components and  $A_0$  is a slowly relaxing exponential tail. The fitted parameters are given in Table S1. At 1.8 K, the total oscillating volume fraction  $A_1 + A_2 = 0.75(6)$  is close to the expected value of  $2/3$  for a fully ordered long-range magnetic system.

In the  $x = 0.3$  sample, two-component Gaussian plus fast exponential spectra are observed at 11 K and 5 K, modeled as

$$a(t) = a_{KT} [A_0 + A_1 \exp(-\lambda_1 t)] \quad (3)$$

and a two-component slow exponential plus fast exponential spectrum at is observed at base temperature given by

$$a(t) = a_0 [A_0 \exp(-\lambda_0 t) + A_1 \exp(-\lambda_1 t)]. \quad (4)$$

The fitted parameters are given in Table S2.

$x = 0.05$	$A_0$	$\lambda_0 (\mu\text{s}^{-1})$	$A_1$	$\lambda_1 (\mu\text{s}^{-1})$	$\omega_1 (\text{MHz})$	$A_2$	$\lambda_2 (\mu\text{s}^{-1})$	$\omega_2 (\text{MHz})$
$T = 11 \text{ K}$	0.543(5)	0.089(3)	0.54(1)	4.1(2)	-	-	-	-
$T = 1.8 \text{ K}$	0.284(4)	0.057(5)	0.37(4)	4.4(4)	2.40(4)	0.41(4)	3.8(4)	0.92(3)

TABLE S1. Fitted parameters of the  $\mu\text{SR}$  spectra of polycrystalline Ru<sub>1-x</sub>Ir<sub>x</sub>Cl<sub>3</sub> with  $x = 0.05$ , see Eqn. (2).

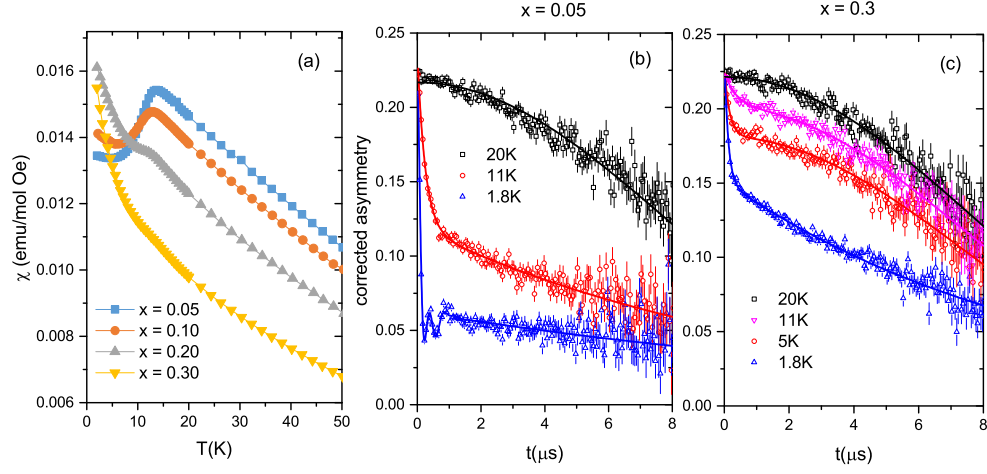


FIG. S7. (a) Magnetic susceptibility curves of  $\text{Ru}_{1-x}\text{Ir}_x\text{Cl}_3$  powders with  $B = 1$  T. Zero-field  $\mu\text{SR}$  spectra at various temperatures in  $\text{Ru}_{1-x}\text{Ir}_x\text{Cl}_3$  powders with (b)  $x = 0.05$  and (c)  $x = 0.30$ . Solid lines are fits to relaxation models described in the text.

$x = 0.30$	$\Delta$	$A_1$	$\lambda_1 (\mu\text{s}^{-1})$	$A_2$	$\lambda_2 (\mu\text{s}^{-1})$
$T = 20\text{ K}$	0.095(9)	-	-	-	-
$T = 11\text{ K}$	0.096(1)	0.109(7)	2.8(4)	0.914(3)	-
$T = 5\text{ K}$	0.097(1)	0.209(1)	6.1(6)	0.823(2)	-
$T = 1.8\text{ K}$	-	0.39(1)	8.6(4)	0.687(3)	0.1007(2)

TABLE S2. Fitted parameters of the  $\mu\text{SR}$  spectra of polycrystalline  $\text{Ru}_{1-x}\text{Ir}_x\text{Cl}_3$  with  $x = 0.3$ , see Eqn. (3)-(4).

## REFERENCES

- [1] H.B. Cao et al., Phys. Rev. B 93, 134423 (2016).
- [2] M. Majumdar et al. Phys. Rev. B 91, 180401(R) (2015).